J Sci Comput (2012) 53:222–247
DOI 10.1007/s10915-012-9578-7

WENO Scheme with Subcell Resolution for Computing Nonconservative Euler Equations with Applications to One-Dimensional Compressible Two-Medium Flows

Tao Xiong · Chi-Wang Shu · Mengping Zhang

Received: 10 November 2011 / Revised: 14 January 2012 / Accepted: 23 January 2012 /
Published online: 4 February 2012

Abstract High order path-conservative schemes have been developed for solving nonconservative hyperbolic systems in (Parés, SIAM J. Numer. Anal. 44:300–321, 2006; Castro et al., Math. Comput. 75:1103–1134, 2006; J. Sci. Comput. 39:67–114, 2009). Recently, it has been observed in (Abgrall and Karni, J. Comput. Phys. 229:2759–2763, 2010) that this approach may have some computational issues and shortcomings. In this paper, a modification to the high order path-conservative scheme in (Castro et al., Math. Comput. 75:1103–1134, 2006) is proposed to improve its computational performance and to overcome some of the shortcomings. This modification is based on the high order finite volume WENO scheme with subcell resolution and it uses an exact Riemann solver to catch the right paths at the discontinuities. An application to one-dimensional compressible two-medium flows of nonconservative or primitive Euler equations is carried out to show the effectiveness of this new approach.

Keywords Path-conservative schemes · High order finite volume WENO scheme · Subcell resolution · Nonconservative hyperbolic systems · Primitive Euler equations · Two-medium flows · Exact Riemann solver

Dedicated to Professor Saul Abarbanel on the occasion of his 80th birthday.

C.-W. Shu was supported by ARO grant W911NF-11-1-0091 and NSF grant DMS-1112700.
M. Zhang was supported by NSFC grant 11071234.

T. Xiong · M. Zhang
School of Mathematical Sciences, University of Science and Technology of China, Hefei, Anhui 230026, P.R. China

T. Xiong
e-mail: jingt@mail.ustc.edu.cn

M. Zhang
e-mail: mpzhang@ustc.edu.cn

C.-W. Shu (✉)
Division of Applied Mathematics, Brown University, Providence, RI 02912, USA
e-mail: shu@dam.brown.edu

1 Introduction

Recent years have seen a growing interest in developing numerical algorithms for solving compressible multicomponent flows. The dynamics of inviscid multicomponent fluid may be modeled by the Euler equations. However, computations often run into unexpected difficulties due to nonphysical oscillations generated at the vicinity of the material interface, while such oscillations do not arise in single-fluid computations when a nonlinearly stable scheme, such as the essentially non-oscillatory (ENO) or weighted ENO (WENO) scheme [18, 22, 32, 41], is used. The underlying mechanisms have been analyzed and several methods have been developed to overcome these difficulties, e.g. in [1, 2, 5, 10, 24, 25, 28].

There are mainly two approaches to circumvent these oscillations. One is still based on the conservative Euler equations, and the other is to write the Euler equations in nonconservative or primitive form.

The ghost fluid method (GFM) developed in [14] with the isobaric fix technique in [15] has provided an attractive and flexible way to treat the two-medium flow model for conservative Euler equations. The GFM treats the material interface as an internal boundary, and by defining ghost cells and ghost fluids, the two-medium flow can be solved via two respective single-medium Riemann problems. This method is simple, can be easily extended to multi-dimensions, and can maintain a sharp interface without oscillations. Variants of the original GFM and their applications can be found in, e.g. [28–30, 49] and the references therein. Later, these techniques are used to develop the Runge-Kutta discontinuous Galerkin (RKDG) finite element method for multi-medium flow in [36, 37, 50, 55]. The GFM, even though approximating directly the conservative Euler equations, is in general not a conservative method because the flux at the interface is double-valued. Recently, a conservative modification to the GFM using the fifth order finite difference WENO scheme with third order Runge-Kutta time discretization has been studied in [31], which attempts to reduce the conservation error of the GFM without affecting its performance.

The other approach is based on the observation that erroneous pressure fluctuations are generated by the conservative equations, hence a better approximation can be obtained when writing the equations in a nonconservative (primitive) form [23, 24]. In these papers a scheme for the nonconservative Euler formulation is proposed, with consistent correction terms to remove the leading order conservation errors. This scheme can completely eliminate spurious oscillations at the material interface, yielding clean monotonic solution profiles. This work has been extended to solve two dimensional problems in [38]. In this method, the correction terms depend heavily on the corresponding conservative numerical scheme. Only second order nonconservative schemes are considered and they are only applied to shocks of weak to moderate strengths. This method is also less justifiable for high-resolution schemes with narrow shock transition and it is not justified in cases of strong shocks [20]. It is noted in these papers that, for nonconservative hyperbolic systems, the shock relationships are not uniquely defined by the limiting left and right states, as they also depend on the viscous path connecting the two states. The correct shock capturing lies in getting correctly the viscous path.

The theory developed by Dal Maso, LeFloch and Murat [12] gives a rigorous definition of nonconservative products, associated with the choice of a family of paths. Later, people have paid much attention to the development of numerical schemes for solving nonconservative hyperbolic systems, see for example [6–8, 35] and references therein. A high order Roe-type scheme based on the reconstructed states has been provided in [7] for the one-dimensional case, and then extended to two dimensions in [6], but only with applications to shallow-water systems. Other work based on this high order method has been carried out

for solving two-phase flow models in [13, 45, 46]. A limitation of this approach has been pointed out recently in [3] when applied to nonconservative Euler equations. The problem is related to the effective choice of a correct path in the nonconservative high order scheme. It appears that, for nonconservative Euler equations, using the Roe linearization to choose a path as in [6, 7, 48] might end up in converging to a weak solution of a different path [3], see also this deficiency in Fig. 3 of our Example 3 in Sect. 8. Several natural questions were raised in [3] for the path-conservative schemes, including (i) how does one go about choosing a path; (ii) what influence does the choice of path and discretization scheme have on the computed solution; (iii) once a path is specified and a consistent path-conservative scheme designed, does the numerical solution converge to the assumed path; and (iv) in cases where the correct jump conditions are known unambiguously, can a path-conservative scheme be designed so that it converges to the correct solution. The answer to (i) is likely to have to come from physics. For a non-conservative formulation of a conservative system, as is the case discussed in this paper, the choice of the path can be achieved by an exact Riemann solver. We attempt to discuss possible approaches to address (ii), (iii) and (iv) in this paper. We focus on adapting high order schemes for solving nonconservative Euler equations, still based on high order Roe-type finite volume schemes as those in [6, 7]. For the nonconservative or primitive Euler equations, the right path should recover the weak solution of the conservative Euler formulation with density, momentum and energy as its variables. In smooth regions, the conservative and nonconservative Euler equations are equivalent, but at discontinuities, they are not [23]. As is well known, shock capturing schemes such as monotone, total variation diminishing (TVD), or ENO and WENO schemes, smear discontinuities with one or several transitional points. These transitional points are necessary for conservation, however in a nonconservative formulation, they may not land on the correct path in the phase space and hence may lead to convergence to erroneous weak solutions on different paths. Realizing this difficulty, which unfortunately is generic with all shock capturing schemes, our basic idea in this paper is to use Harten's subcell resolution technique [17] to sharpen the discontinuities and effectively eliminate (or at least significantly reduce) the transitional points. As a result, the convergence towards the correct weak solution based on the originally desired path seems to be restored.

Harten's subcell resolution idea [17] is based on ENO schemes with a Lax-Wendroff time discretization procedure in a cell-averaged framework. Later, this idea is extended in [42] to both finite volume and finite difference ENO schemes with Runge-Kutta time discretization. Recently, this subcell resolution idea has been used in solving advection equations with stiff source terms, to obtain correct shock speed on coarse meshes [51]. In this paper, with the sharp left and right states at the discontinuities, we use an exact Riemann solution to catch the right path that connects the two states, as the correct capturing of the shock speed is sensitive to the accuracy of the numerically achieved path. Numerical experiments for one-dimensional compressible one- and two-medium flows of nonconservative Euler equations show the effectiveness of our new approach. Based on these results, we give partial answers to the questions in [3] as quoted above: (i) at least for nonconservative or primitive Euler equations, the right path should recover the weak solution of the conservative Euler formulation with density, momentum and energy as its variables; (ii) at least for nonconservative Euler equations, different paths would lead to very different weak solutions; (iii) numerical solution from a path-conservative scheme designed for a specified path, with a smeared shock front, does not necessarily converge to the weak solution corresponding to the desired path, see for example Fig. 3 in Sect. 8; (iv) at least for the nonconservative Euler equations, where we know the correct jump conditions, our approach of high order Roe path-conservative scheme with subcell resolution can effectively remove smearing of discontinuities, leading to convergence to the correct solution.

This paper is organized with the following sections. In Sect. 2, we first describe the high order Roe scheme for the nonconservative hyperbolic systems. Then we introduce the two-medium flow model for nonconservative Euler equations in Sect. 3. In Sect. 4, we illustrate how to apply the WENO reconstruction with subcell resolution to the high order Roe scheme. In Sect. 5, we describe the computation of the integral term in the high order Roe scheme in detail. In Sect. 6, we present the level set function to track the material interface. A summary of our algorithm to aid implementation is given in Sect. 7, and one-dimensional numerical examples are provided to demonstrate the effectiveness of our approach in Sect. 8. Concluding remarks follow in the last section.

2 High Order Roe Scheme for Nonconservative Hyperbolic Systems

In this section, we follow the procedure in [7] to define the high order Roe scheme for solving nonconservative hyperbolic systems. For the one-dimensional case, a nonconservative hyperbolic system reads

$$W_t + A(W)W_x = 0, \quad x \in \Omega \subset \mathbb{R},\ t > 0 \tag{2.1}$$

where $W = W(x,t)$ is a N-component state vector and $A(W)$ is a $N \times N$ matrix. The system is supposed to be hyperbolic, i.e. $A(W)$ has N real eigenvalues and a full set of N linearly independent eigenvectors.

For simplicity, we use a uniform grid

$$a = x_{\frac{1}{2}} < x_{\frac{3}{2}} < \cdots < x_{N_x-\frac{1}{2}} < x_{N_x+\frac{1}{2}} = b.$$

The cells, cell centers, and the uniform cell size are denoted by

$$I_i \equiv [x_{i-\frac{1}{2}}, x_{i+\frac{1}{2}}], \qquad x_i \equiv \frac{1}{2}(x_{i-\frac{1}{2}} + x_{i+\frac{1}{2}}), \qquad \Delta x \equiv x_{i+\frac{1}{2}} - x_{i-\frac{1}{2}}, \quad i = 1, 2, \ldots, N_x.$$

In the case of systems of conservation laws, that is when $A(W) = \partial F/\partial W$, which is the Jacobian of a flux function $F(W)$, (2.1) reduces to a classical conservation law

$$W_t + F(W)_x = 0. \tag{2.2}$$

A conservative finite volume semi-discretization [26] of the system (2.2) is

$$W_i'(t) = \frac{1}{\Delta x}(G_{i-1/2} - G_{i+1/2}), \tag{2.3}$$

with the numerical flux

$$G_{i+1/2} = G\big(W^-_{i+1/2}(t), W^+_{i+1/2}(t)\big), \tag{2.4}$$

where $W_i(t)$ is used to approximate the cell averaged value $\overline{W}_i(t)$, which is defined as

$$\overline{W}_i(t) = \frac{1}{\Delta x}\int_{x_{i-1/2}}^{x_{i+1/2}} W(x,t)dx,$$

and $W^{\pm}_{i+1/2}(t)$ are the left and right limits of solutions at the cell boundary $x_{i+1/2}$, which are the reconstructed states associated to the cell average sequence $\{W_j(t)\}$.

The semi-discrete high order Roe scheme for (2.3) can be written as

$$W_i'(t) = -\frac{1}{\Delta x}\big(A^+_{i-1/2}\big(W^+_{i-1/2}(t) - W^-_{i-1/2}(t)\big) + A^-_{i+1/2}\big(W^+_{i+1/2}(t) - W^-_{i+1/2}(t)\big) - F\big(W^+_{i-1/2}(t)\big) + F\big(W^-_{i+1/2}(t)\big)\big) \tag{2.5}$$

which is equivalent to the conservative scheme (2.3) with the numerical flux (2.4) defined to be

$$\begin{aligned} G_{i+1/2} &= F\big(W^-_{i+1/2}(t)\big) + A^-_{i+1/2}\big(W^+_{i+1/2}(t) - W^-_{i+1/2}(t)\big) \\ &= F\big(W^+_{i+1/2}(t)\big) - A^+_{i+1/2}\big(W^+_{i+1/2}(t) - W^-_{i+1/2}(t)\big) \\ &= \frac{1}{2}\big(F\big(W^+_{i+1/2}(t)\big) + F\big(W^-_{i+1/2}(t)\big) - |A_{i+1/2}|\big(W^+_{i+1/2}(t) - W^-_{i+1/2}(t)\big)\big). \end{aligned} \tag{2.6}$$

Here

$$|A_{i+1/2}| = A^+_{i+1/2} - A^-_{i+1/2} \tag{2.7}$$

and the Roe property

$$A_{i+1/2}\big(W^+_{i+1/2}(t) - W^-_{i+1/2}(t)\big) = F\big(W^+_{i+1/2}(t)\big) - F\big(W^-_{i+1/2}(t)\big) \tag{2.8}$$

has been used. The intermediate matrices are defined by

$$A_{i+1/2} = \hat{A}\big(W^+_{i+1/2}(t), W^-_{i+1/2}(t)\big) \tag{2.9}$$

and

$$A^\pm_{i+1/2} = R_{i+1/2}\Lambda^\pm_{i+1/2}R^{-1}_{i+1/2}, \qquad \Lambda^\pm_{i+1/2} = \operatorname{diag}\big((\lambda_1)^\pm_{i+1/2}, \ldots, (\lambda_N)^\pm_{i+1/2}\big) \tag{2.10}$$

where $R_{i+1/2}$ is a $N \times N$ matrix with each column as a right eigenvector of $A_{i+1/2}$, and $\Lambda_{i+1/2}$ is the diagonal matrix whose diagonal entries are the corresponding eigenvalues of $A_{i+1/2}$. We have $\hat{A}(W, W) = A(W)$, and a specific definition of (2.9) is given in Sect. 4. In (2.10), we define

$$(x)^+ = \begin{cases} x, & \text{if } x > 0 \\ 0, & \text{otherwise} \end{cases} \qquad (x)^- = \begin{cases} x, & \text{if } x < 0 \\ 0, & \text{otherwise} \end{cases}$$

so $\Lambda^\pm_{i+1/2}$ are the corresponding diagonal matrices with positive or negative eigenvalues.

We introduce $P^t_i(x)$ as any smooth function defined in the cell I_i, such that

$$\lim_{x \to x^+_{i-1/2}} P^t_i(x) = W^+_{i-1/2}(t), \qquad \lim_{x \to x^-_{i+1/2}} P^t_i(x) = W^-_{i+1/2}(t). \tag{2.11}$$

Then, (2.5) can be rewritten as

$$W_i'(t) = -\frac{1}{\Delta x}\left(A^+_{i-1/2}\big(W^+_{i-1/2}(t) - W^-_{i-1/2}(t)\big) + A^-_{i+1/2}\big(W^+_{i+1/2}(t) - W^-_{i+1/2}(t)\big) + \int_{x_{i-1/2}}^{x_{i+1/2}} \frac{d}{dx} F\big(P^t_i(x)\big)\,dx\right). \tag{2.12}$$

Now the numerical high order Roe scheme for solving the nonconservative system (2.1) can be easily generalized from (2.12)

$$W_i'(t) = -\frac{1}{\Delta x}\Big(A^+_{i-1/2}\big(W^+_{i-1/2}(t) - W^-_{i-1/2}(t)\big) + A^-_{i+1/2}\big(W^+_{i+1/2}(t) - W^-_{i+1/2}(t)\big) + \int_{x_{i-1/2}}^{x_{i+1/2}} A\big(P_i^t(x)\big)\frac{d}{dx}P_i^t(x)dx\Big) \quad (2.13)$$

with the function $P_i^t(x)$ satisfying (2.11). In order to obtain entropy-satisfying solutions, the Harten-Hyman entropy fix technique [19, 47] can be applied to this scheme.

3 Two-Medium Flow Model for Nonconservative Euler Equations

In this section, we describe the two-medium inviscid compressible flow model for the nonconservative or primitive Euler equations. As pointed out in [23], the choice of the primitive set of variables, that include density, velocity and pressure, provides a model better suited than the conserved variables for computations of propagating material fronts. Such model results in clean and monotonic solution profiles, so we consider the one-dimensional primitive Euler equations

$$W_t + A(W)W_x = 0 \quad (3.1)$$

with

$$W = (\rho, u, p)^T, \qquad A(W) = \begin{pmatrix} u & \rho & 0 \\ 0 & u & \rho^{-1} \\ 0 & \gamma p & u \end{pmatrix}. \quad (3.2)$$

Here ρ is the density, u is the velocity, p is the pressure, γ is the ratio of specific heats. The total energy is given by $E = \rho e + \frac{1}{2}\rho u^2$, where e is the specific internal energy per unit mass. In Sect. 8, we will consider systems of two gases and systems involving air and water. We will use the following γ-law equation of state (EOS) for both air and water

$$\rho e = p/(\gamma - 1) \quad (3.3)$$

note that for the water medium, what we have actually used is the Tait EOS [9, 14, 28, 36], and we need to use $\bar{p} = p + \gamma\bar{B}$ instead of p in all the above formulae, where $\bar{B} = B - A$, $A = 1.0E5$ Pa and $B = 3.31E8$ Pa. For water, $\gamma = 7.15$, and the displayed pressure for the water in Sect. 8 is p, not $\bar{p}$.

4 WENO Reconstruction with Subcell Resolution

In this section, we will describe how to use the WENO reconstruction with subcell resolution to reconstruct $W^{\pm}_{i+1/2}(t)$ from the cell averages $\{W_j(t)\}$. The WENO reconstruction is described in detail in [22, 40]. We follow the procedure in [42] to describe how to apply the subcell resolution technique of Harten [17] to the scheme (2.13) with the third order total variation diminishing (TVD) Runge-Kutta time discretization [41], also called strong stability preserving (SSP) time discretization [16].

We first consider the 1D, scalar, linear version $u_t + f(u)_x = 0$, with $f(u) = au$ and $a > 0$, to describe the WENO reconstruction with the subcell resolution technique. The extension to the nonlinear and system cases will follow. We would like to reconstruct $u^-_{i+1/2}$ and $u^+_{i-1/2}$ in each cell from the sequence of cell averages $\{\overline{u}_j\}$, with the following algorithm.

WENO Reconstruction Algorithm Given the cell averages $\{\overline{u}_j\}$ of a function $u(x)$:

$$\overline{u}_j = \frac{1}{\Delta x}\int_{x_{j-1/2}}^{x_{j+1/2}} u(\xi)d\xi, \quad j = 1, 2, \ldots, N_x, \tag{4.1}$$

based on the big stencil $S_i \equiv \{I_{i-r}, \ldots, I_i, \ldots, I_{i+r}\}$, a k-th ($k = 2r + 1$) order accurate approximation to the boundary values $u^-_{i+1/2}$ and $u^+_{i-1/2}$ in the cell I_i is reconstructed as

$$u^-_{i+1/2} = \sum_{j=0}^{r} \omega_j(x_{i+1/2}) p_j(x_{i+1/2}), \qquad u^+_{i-1/2} = \sum_{j=0}^{r} \omega_j(x_{i-1/2}) p_j(x_{i-1/2}) \tag{4.2}$$

where each $p_j(x)$ is a reconstruction polynomial that uses the cell averages in the small stencil $S^j_i \equiv \{I_{i-j}, \ldots, I_{i-j+r}\} \subset S_i$. The nonlinear weights $\{\omega_j(x)\}^r_{j=0}$ are calculated from the polynomials $\{p_j(x)\}^r_{j=0}$ and the linear weights $\{d_j(x)\}^r_{j=0}$ at each fixed point x, and they satisfy

$$\omega_j(x) > 0, \quad \sum_{j=0}^{r} \omega_j(x) = 1. \tag{4.3}$$

The nonlinear weight $\omega_j(x)$ is close to zero when a discontinuity is located in the stencil S^j_i, so as to avoid involving much information from any stencil S^j_i which contains discontinuities.

Remark For the cell boundaries (4.2), the linear weights $d_j(x_{i+1/2})$ and $d_j(x_{i-1/2})$ are positive. However, at certain internal points $x \in I_i$ (reconstruction at those points are needed in Sect. 5), the linear weights $d_j(x)$ may be negative. The linear weights may also become negative if the stencil S_i is changed to S_{i+1} or S_{i-1}, while still reconstructing values in the cell I_i (e.g. in the following subcell resolution algorithm). In these cases, the technique to treat negative weights in [39] needs to be applied.

Subcell Resolution Algorithm We describe the procedure for the three-stage third order TVD time discretization, specifically given as (7.1) in Sect. 7. First, at the beginning of every Runge-Kutta stage:

(I) Define the "critical intervals" (intervals containing discontinuities) $I_i = (x_{i-1/2}, x_{i+1/2})$ by $\sigma_i \geq \sigma_{i+1}$, $\sigma_i > \sigma_{i-1}$, where $\sigma_i = |m(\Delta_+\overline{u}_i, \Delta_-\overline{u}_i)|$, $\Delta_+\overline{u}_i = \overline{u}_{i+1} - \overline{u}_i$, $\Delta_-\overline{u}_i = \overline{u}_i - \overline{u}_{i-1}$ and m is the minmod function which is defined to be

$$m(a_1, \ldots, a_n) = \begin{cases} s \min_{1\leq i\leq n} |a_i|, & \text{if } s = \text{sign}(a_1) = \cdots = \text{sign}(a_n) \\ 0, & \text{otherwise.} \end{cases} \tag{4.4}$$

(II) For any "critical interval" I_i, let $\theta_i = (\overline{u}_{i+1} - \overline{u}_i)/(\overline{u}_{i+1} - \overline{u}_{i-1})$, and use $x_{i-1/2} + \theta_i \Delta x$ as an approximation to the discontinuity location inside the cell I_i.

Then, in each Runge-Kutta time stage, we perform:

(III) Let the cell I_i boundary values $u^-_{i+1/2}$ and $u^+_{i-1/2}$ be defined as usual, using the standard WENO reconstruction algorithm (4.2), unless I_i or (for the second and third Runge-Kutta stages) I_{i-1} is a "critical interval". If I_i is a "critical interval", we define

$$u^-_{i+1/2} = (1-\xi_i)u^{(L)}_{i+1/2} + \xi_i u^{(R)}_{i+1/2}, \quad \text{with } \xi_i = \min\left(\frac{(1-\theta_i)\Delta x}{a\Delta t}, 1\right) \tag{4.5}$$

$$u^+_{i-1/2} = u^{-,old}_{i-1/2} \tag{4.6}$$

where $u^{-,old}_{i-1/2}$ is the standard WENO reconstruction with the stencil S_{i-1}, $u^{(L)}_{i+1/2}$ is also the standard WENO reconstruction with the stencil S_{i-1}, but evaluated at $x_{i+1/2}$ of the cell I_i, and $u^{(R)}_{i+1/2}$ is the WENO reconstruction with the stencil S_{i+1} and evaluated at $x_{i+1/2}$. Notice that here for $u^{(L)}_{i+1/2}$ the technique for treating negative weights needs to be used. For the second and third Runge-Kutta stages, we choose the stencil S_{i+2} for $u^{(R)}_{i+1/2}$ if $\xi_i < 1$ and the negative weight treating technique needs to be used here as well. When I_{i-1} is a "critical interval" and $\xi_{i-1} < 1$, we choose the stencil S_{i+1} for $u^-_{i+1/2}$.

Remark (a) The case for $a < 0$ is easily obtained by symmetry.

(b) For nonlinear systems, the subcell resolution algorithm is simply applied in each local characteristic field. The detailed procedure can be found in [42]. The only difference in our current situation is that we just use $A(W_i(t))$ to do the characteristic decomposition when defining if I_i is a "critical interval". However if the material interface is located in the cell I_i, we always set it to be a "critical interval", and we use $A(\frac{W_i(t)+W_{i+1}(t)}{2})$ to do the characteristic decomposition for the right cell boundary at $x_{i+1/2}$, and $A(\frac{W_{i-1}(t)+W_i(t)}{2})$ for the left cell boundary at $x_{i-1/2}$. The average to define the intermediate matrix in (2.9) is

$$A_{i+1/2} = \hat{A}\big(W^+_{i+1/2}(t), W^-_{i+1/2}(t)\big) = A\left(\frac{W^+_{i+1/2}(t) + W^-_{i+1/2}(t)}{2}\right).$$

(c) For systems, due to different local characteristic decomposition, two adjacent cells might both be "critical intervals". In this situation, we remove the one with a smaller σ_i from the list of critical intervals.

(d) It is pointed out in [17, 42] that the subcell resolution technique should be applied only to sharpen contact discontinuities. Special caution is needed when one tries to sharpen a (nonlinear) shock, to avoid obtaining a nonphysical, entropy condition violating solution. In our approach, the subcell resolution is used to get sharp left and right states at the discontinuities. At a nonlinear shock, this is also needed so as to get a more accurate shock speed which heavily depends on the left and right states. In the computation for Euler equations of compressible gas dynamics, we apply the subcell resolution algorithm in both the linearly degenerate field and genuinely nonlinear fields [47], but for the genuinely nonlinear fields, with eigenvalues λ^L and λ^R corresponding to the left and right states respectively, we only apply the subcell resolution for the case $\lambda^L \geq \lambda^R$ to avoid sharpening a rarefaction wave.

5 Choice of the Path and Evaluation of the Path Integral

In smooth regions, all simple wave models for conservative Euler equations and primitive Euler equations are equivalent. However, near discontinuities, they are not equivalent [23]. According to this, our choice of the path is divided into three parts: the smooth case, discontinuities in a single medium, and discontinuities at the material interface.

5.1 The Smooth Case

In the smooth case, the integral term in (2.13)

$$\int_{x_{i-1/2}}^{x_{i+1/2}} A\big(P_i^t(x)\big)\frac{d}{dx}P_i^t(x)dx \tag{5.1}$$

can be computed via a high order accurate Gauss-Lobatto quadrature rule. Given the positions $\{s_j\}$ and associated weights $\{\omega_j\}$ for a G-point quadrature in the interval $[-\frac{1}{2},\frac{1}{2}]$, we can replace the analytical path integral (5.1) by

$$\int_{x_{i-1/2}}^{x_{i+1/2}} A\big(P_i^t(x)\big)\frac{d}{dx}P_i^t(x)dx \approx \sum_{j=1}^{G}\omega_j A\big(P_i^t(s_j)\big)\frac{d}{dx}P_i^t(s_j). \tag{5.2}$$

In our numerical experiments, we use the four-point Gauss-Lobatto quadrature rule:

$$s_{1,4}=\mp\frac{1}{2},\qquad s_{2,3}=\mp\frac{\sqrt{5}}{10},\qquad \omega_{1,4}=\frac{1}{6},\qquad \omega_{2,3}=\frac{5}{6}. \tag{5.3}$$

For $P_i^t(s_{1,4})$, from (2.11) we already have

$$P_i^t(s_1)=W_{i-1/2}^+,\qquad P_i^t(s_4)=W_{i+1/2}^- \tag{5.4}$$

following the same procedure for obtaining $P_i^t(s_{1,4})$, we can also obtain $P_i^t(s_{2,3})$, where $P_i^t(s_2)$ is obtained in the same way as $P_i^t(s_1)$ corresponding to the local characteristic field at $x_{i-1/2}$, and $P_i^t(s_3)$ as $P_i^t(s_4)$ corresponding to the local characteristic field at $x_{i+1/2}$. Note here for the smooth case, we do not need the subcell resolution in the WENO reconstruction. Since we have $\{P_i^t(s_j)\}_{j=1}^4$, $\frac{d}{dx}P_i^t(x)$ can be approximated by $Q(x)$, the derivative of the Lagrangian interpolation polynomial based on $\{P_i^t(s_j)\}_{j=1}^4$. Then $\frac{d}{dx}P_i^t(s_j)$ can be replaced by $Q(s_j)$ in (5.2).

5.2 Discontinuities in a Single Medium

At the discontinuities, the cell is defined as a "critical interval", and we have obtained the left and right states $W_{i-1/2}^+$ and $W_{i+1/2}^-$ from the WENO reconstruction with subcell resolution in Sect. 4. Denote the left and right states $W_{i-1/2}^+$ and $W_{i+1/2}^-$ to be W_L and W_R, we can use the exact Riemann solver [43, 47] to obtain the exact Riemann solution between the two states. The exact Riemann solution for the compressible Euler equations contains four constant states connected by a rarefaction wave or a shock wave, a contact discontinuity, and another rarefaction wave or shock wave. The four constant states can be denoted as W_L, W_{*L}, W_{*R} and W_R. In this case of the "critical interval", we use the exact Riemann solution to get the integral path for the integral term (5.1). It can be computed as the following seven parts:

(a) The four constant-state parts, since $\frac{d}{dx}P_i^t(x)=0$, the integral in these four parts are all zero.

(b) If W_L and W_{*L} are connected by a rarefaction wave, we similarly use the 4-point Gauss-Lobatto quadrature rule (5.3), and $P_i^t(x)$ in this part is just the rarefaction wave line. Otherwise, if W_L and W_{*L} are connected by a shock wave, then the integral path for this part needs to satisfy the Rankine-Hugoniot jump condition of the conservative Euler equations, and the integral result is $\sigma(W_{*L}-W_L)$, with σ being the shock speed related to the two states W_L and W_{*L}. Similar results can be obtained for the connection between W_{*R} and W_R.

(c) For the contact discontinuity part between W_{*L} and W_{*R}, the integral path also needs to satisfy the Rankine-Hugoniot jump condition. Since W_{*L} and W_{*R} have the same pressure p and velocity u and different densities ρ_{*L} and ρ_{*R}, the integral result is simply $(u(\rho_{*R} - \rho_{*L}), 0, 0)^T$.

Remark In (b) and (c) above, for the shock wave and contact discontinuity, we do not need to know the exact integral paths for satisfying the Rankine-Hugoniot jump condition, in order to get the integral results along those paths. We only need to make sure that these paths exist, which can be easily verified.

5.3 Discontinuities at the Material Interface

We always set the cell at the material interface as a "critical interval". The integral term (5.1) can be computed similar to the second case of discontinuities in a single medium, as the exact Riemann solution at the material interface is almost the same as that for the single-component compressible Euler equations, also containing four constant states connected by a rarefaction wave or a shock wave, a contact discontinuity, and another rarefaction wave or shock wave [27, 28, 30]. Apart from W_{*L} and W_{*R} which are connected by a contact discontinuity, the left part is for medium one with the ratio of specific heats γ_1 and the right part is for medium two with the ratio of specific heats γ_2.

6 Tracking the Moving Medium Interface

In this section, we describe how to use the level set equation [4, 34, 44] to track the moving fluid interface. The level set equation for the one-dimensional case is

$$\phi_t + u\phi_x = 0. \tag{6.1}$$

The interface is tracked as the zero level set of ϕ, with the initialized $\phi(x)$ to be the signed normal distance to the material front. We use a fifth order finite difference WENO method [22, 40] with the third order TVD Runge-Kutta time discretization [41] to solve the level set equation (6.1). This equation is solved concurrently with the nonconservative Euler equations (3.1), using the velocity u coming from the Euler equations. The solution $\phi = \phi_0$ from solving the level set equation (6.1) has the zero level set as the material interface, but it does not need to be the distance function for $t > 0$. A serious distorted level set function $\phi = \phi_0$ may lead to significant errors for $t > 0$. For this reason, $\phi_0(x)$ is reinitialized to be a signed normal distance function to the interface by solving the following eikonal equation to steady state

$$\phi_\tau = S(\phi_0)(1 - |\phi_x|) \tag{6.2}$$

through iterating the pseudo-time τ, where $S(\phi) = \frac{\phi}{\sqrt{\phi^2+(\Delta x)^2}}$ is the approximate sign function. We use the Godunov Hamiltonian and the fifth order finite difference WENO discretization in [21, 54] to solve (6.2). The stopping criterion for this iteration is $e_1 < \Delta\tau(\Delta x)^2$, where e_1 is the L^1 difference of ϕ between two consecutive iteration steps, and we take $\Delta\tau = \Delta x/10$ in the experiments [44].

7 Algorithm Summary

Our basic semi-discrete scheme is (2.13), which can be written as

$$W_t = L(W).$$

It is discretized in time by the third order TVD Runge-Kutta method [41], also referred to as the SSP Runge-Kutta method SSPRK(3,3) [16]:

$$\begin{aligned} W^{(1)} &= W^n + \Delta t L\big(W^n\big), \\ W^{(2)} &= \frac{3}{4}W^n + \frac{1}{4}W^{(1)} + \frac{1}{4}\Delta t L\big(W^{(1)}\big), \\ W^{n+1} &= \frac{1}{3}W^n + \frac{2}{3}W^{(2)} + \frac{2}{3}\Delta t L\big(W^{(2)}\big). \end{aligned} \tag{7.1}$$

Notice that this high order SSP Runge-Kutta method is simply a convex combination of three Euler forwards. We can now summarize our algorithm to advance one time step (from t^n to t^{n+1}) in the following steps.

Step 1. Compute the new time step size based on the CFL condition:

$$\Delta t = \mathrm{CFL}\,\Delta x / \max_{1\le j\le N_x}\left(|u_j^n| + c_j^n\right) \tag{7.2}$$

where $c_j^n = \sqrt{\gamma p_j^n/\rho_j^n}$ is the sound speed, and ρ_j^n, u_j^n, p_j^n are the density, velocity and pressure at time level t^n, respectively. This step needs to be done only at the beginning of the whole Runge-Kutta step.

Step 2. Taking W^n and ϕ^n as the initial condition, solve

$$W_t = L(W), \tag{7.3}$$

$$\phi_t = P(\phi), \tag{7.4}$$

for one time step using the Runge-Kutta time discretization (7.1). Here (7.4) is written from (6.1) with the fifth order finite difference WENO spatial discretization. At each Runge-Kutta time stage, we first reconstruct $W^+_{i-1/2}$ and $W^-_{i+1/2}$ as described in Sect. 4, then, based on $W^+_{i-1/2}$ and $W^-_{i+1/2}$, we compute the integral term (5.1) as described in Sect. 5. We can then formulate the right side of (7.3). $P(\phi)$ can be formulated simultaneously, given the velocity $u = u^n$ from the Euler equations. Denote the updated W by W^{n+1}, and the updated ϕ by $\tilde{\phi}^{n+1}$.

Step 3. Reinitialize $\tilde{\phi}^{n+1}$ by solving (6.2) with $\phi_0 = \tilde{\phi}^{n+1}$, and denote this solution by ϕ^{n+1}.

Step 4. Define the new interface position from the zero level set of ϕ^{n+1}. Now we have advanced one time step.

8 Numerical Experiments

In the following, we show several one-dimensional numerical examples to demonstrate that our approach can improve the performance of the high order Roe scheme for the nonconservative Euler equations. With fifth order WENO reconstruction in Sect. 4 ($r = 2$) and

Table 1 Accuracy test for Example 1 with initial data (8.1), $t = 1$. Without subcell resolution

N_x	L^1 error	Order	L^∞ error	Order
20	2.01E–04	–	3.73E–04	–
40	5.95E–06	5.08	1.28E–05	4.86
80	1.81E–07	5.04	3.93E–07	5.02
160	5.58E–09	5.02	1.19E–08	5.05
320	1.76E–10	4.99	3.53E–10	5.07

Table 2 Accuracy test for Example 1 with initial data (8.1), $t = 1$. With subcell resolution

N_x	L^1 error	Order	L^∞ error	Order
20	4.03E–04	–	7.20E–04	–
40	1.45E–05	4.80	4.83E–05	3.90
80	4.30E–07	5.07	3.00E–06	4.01
160	1.39E–08	4.95	1.46E–07	4.36
320	4.16E–10	5.06	7.92E–09	4.20

four-point Gauss-Lobatto quadrature rule in Sect. 5.1, the Roe scheme can achieve fifth order accuracy for smooth solutions, which will be tested in Example 1. Except for Example 1, Example 3 and Example 5, the computational domain for all other examples are taken as [0, 1], and the initial material interface for the two-medium flow problems is located at $x = 0.5$. Due to the need of good performance for the subcell resolution in the Runge-Kutta context, we take a small CFL number 0.1 for all examples [42]. The computational domain is divided with $N_x = 100$ uniform grids. Units for density, velocity, pressure, length and time are kg/m^3, m/s, Pa, m and s, respectively.

Example 1 In this example, we first test the accuracy for a smooth solution to a single component nonconservative Euler equations with initial conditions

$$\rho_0(x) = 1 + 0.8\sin(x), \qquad u_0(x) = 1, \qquad p_0(x) = 1 \tag{8.1}$$

on a domain $[0,\ 2\pi]$ with periodic boundary conditions. The exact solution is

$$\rho(x) = 1 + 0.8\sin(x - t), \qquad u(x) = 1, \qquad p(x) = 1.$$

Since the solution to this problem is smooth, theoretically we do not need to apply the subcell resolution. We use fifth order WENO reconstruction in Sect. 4 ($r = 2$) and four-point Gauss-Lobatto quadrature rule for the integral term in the smooth case in Sect. 5.1. Without subcell resolution, the fifth order accuracy for both L^1 and L^∞ norms can be achieved for this path-conservative scheme applied to the single-component nonconservative Euler equations, as listed in Table 1. If we apply the subcell resolution in the tracked critical intervals, we can also obtain fifth order accuracy for the L^1 norm, but we lose one order for the L^∞ norm, as listed in Table 2. This is reasonable as we would have only applied the subcell resolution in a few cells in this one-dimensional case, and treating the smooth cells as discontinuous cells would cause some loss of accuracy in these cells.

Example 2 In this example, we now show a single-medium flow problem, which is the standard Lax shock tube problem, to demonstrate that we obtain the correct entropy solution by our nonconservative scheme. Here $\gamma = 1.4$ is used, with the initial condition:

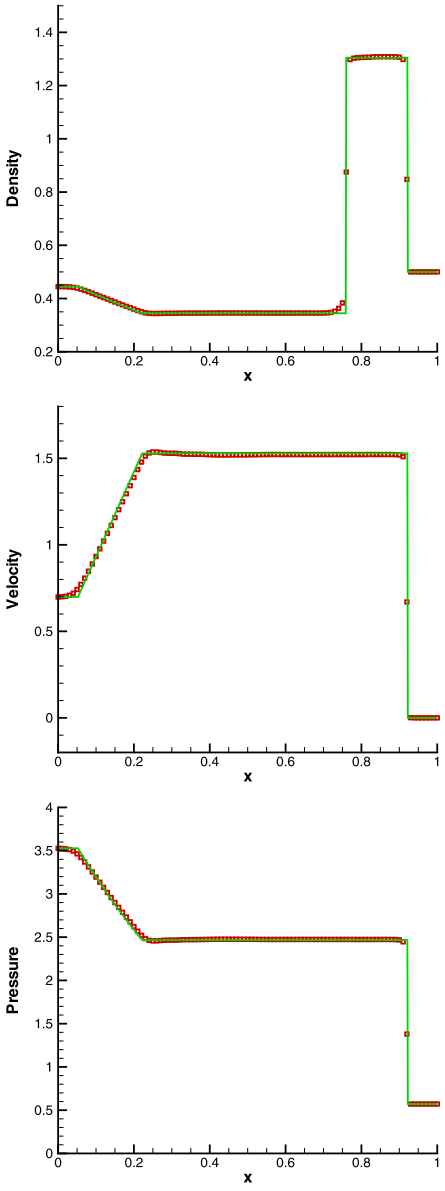

Fig. 1 Density, velocity and pressure for Example 2. $t = 0.17$. *Solid line*: the exact solution. *Symbol*: the numerical solution

$$(\rho, u, p) = \begin{cases} (0.445, 0.698, 3.528) & \text{for } x \leq 0.5; \\ (0.5, 0, 0.571) & \text{for } x > 0.5. \end{cases} \tag{8.2}$$

The computed density ρ, velocity u and pressure p are plotted at $t = 0.17$ against the exact solution in Fig. 1. We can see that the rarefaction wave, contact discontinuity and shock wave are all captured well.

Example 3 This example is a right moving shock for a single-medium flow. Here $\gamma = 5/3$ is used, with the initial condition:

$$(\rho, u, p) = \begin{cases} (\frac{41}{14}, 9\sqrt{\frac{3}{41}}, 10) & \text{for } x \le 0.5; \\ (1, 0, 1) & \text{for } x > 0.5. \end{cases} \tag{8.3}$$

We compute this problem on a domain $[0, 1]$. A similar example (in Lagrangian form) is used in [3] to demonstrate potential problems of nonconservative path-based Roe-type and Lax-Friedrichs (LxF)-type schemes. The computed density ρ, velocity u and pressure p are plotted at $t = 0.1$ against the exact solution in Fig. 2. We can see that our algorithm can capture the correct shock location in this case, and the minor glitches on the left constant state would not grow with a much refined mesh (figures on the right).

We also use this simple example to illustrate that in our approach, the subcell resolution and the exact Riemann solution are both necessary in order to catch the right path in this nonconservative scheme. In Fig. 3, we list the results for two cases: one is obtained when we use the exact Riemann solution but without subcell resolution, the other is obtained when we use subcell resolution but with the line path [3, 48] instead of the exact Riemann solution, on a very refined mesh $N_x = 1000$. We can see that neither of them can catch the correct shock solution.

Example 4 This is an air-helium shock tube problem taken from [14, 31, 36], with the initial condition:

$$(\rho, u, p, \gamma) = \begin{cases} (1, 0, 1 \times 10^5, 1.4) & \text{for } x \le 0.5; \\ (0.125, 0, 1 \times 10^4, 1.2) & \text{for } x > 0.5. \end{cases} \tag{8.4}$$

The computed density ρ, velocity u and pressure p are plotted at $t = 0.0007$ running with 495 time steps in our code, against the exact solution in Fig. 4. We can see that the rarefaction wave, the contact discontinuity and the shock wave are all captured well for this two-medium flow.

Example 5 This example is used to demonstrate the advantage of high order methods as in [50] for two-medium flows. It contains both shocks and fine structures in smooth regions, which is a simple model for shock-turbulence interactions. The initial discontinuity is right on the material interface and located at $x = -4$, the left and right states for the initial discontinuity are

$$(\rho, u, p, \gamma) = \begin{cases} (3.857143, 2.629369, 10.333333, 1.4) & \text{for } x < -4, \\ (1 + 0.2\sin(5x), 0, 1, 5/3) & \text{for } x > -4. \end{cases} \tag{8.5}$$

We compute the example up to time $t = 1.8$ on a domain $[-5,\ 5]$. For comparison, we also show the results obtained with a second order method, by replacing the fifth order WENO reconstruction with subcell resolution in Sect. 4 with a second order ENO reconstruction [17, 42], and replacing the four-point Gauss-Lobatto quadrature rule for the smooth integral term in Sect. 5.1 with a trapezoid rule. We plot the densities obtained by the second order and the fifth order methods with $N_x = 200$ in Fig. 5. The solid line is the solution obtained by the fifth order method with $N_x = 1000$ points, which can be considered as a converged reference solution. We can find that the two methods can both capture the correct solution. However the result of the fifth order method is in better agreement with the converged reference

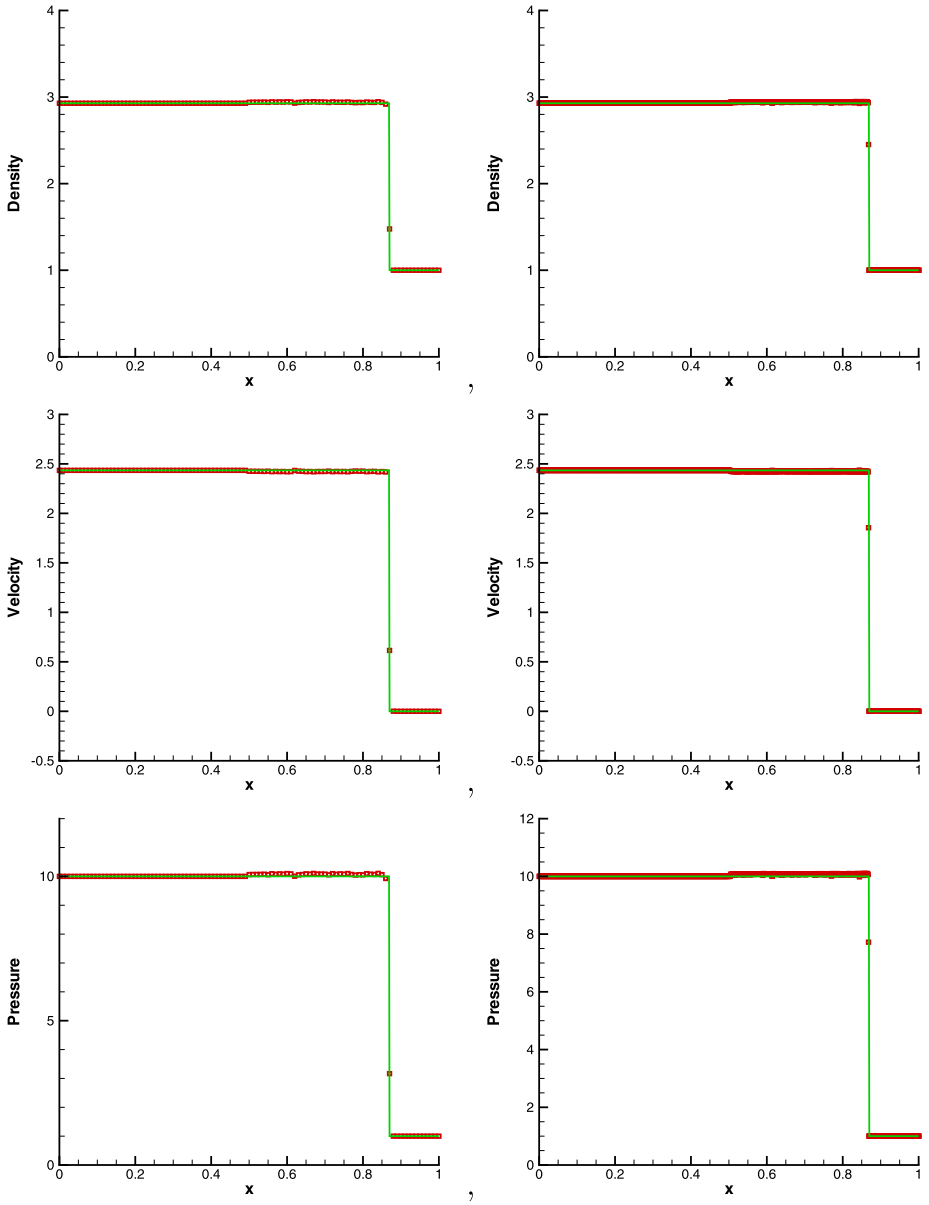

Fig. 2 Density, velocity and pressure for Example 3. $t = 0.1$. *Solid line*: the exact solution. *Symbol*: the numerical solution. *Left*: mesh $N_x = 100$; *Right*: mesh $N_x = 1000$

solution than the second order method, especially in the region with fine structures, on this relatively coarse mesh. This is similar to the results in [50].

Example 6 This is a problem of a shock wave refracting at an air-helium interface with a reflected weak rarefaction wave taken from [14, 31, 36], with the initial condition:

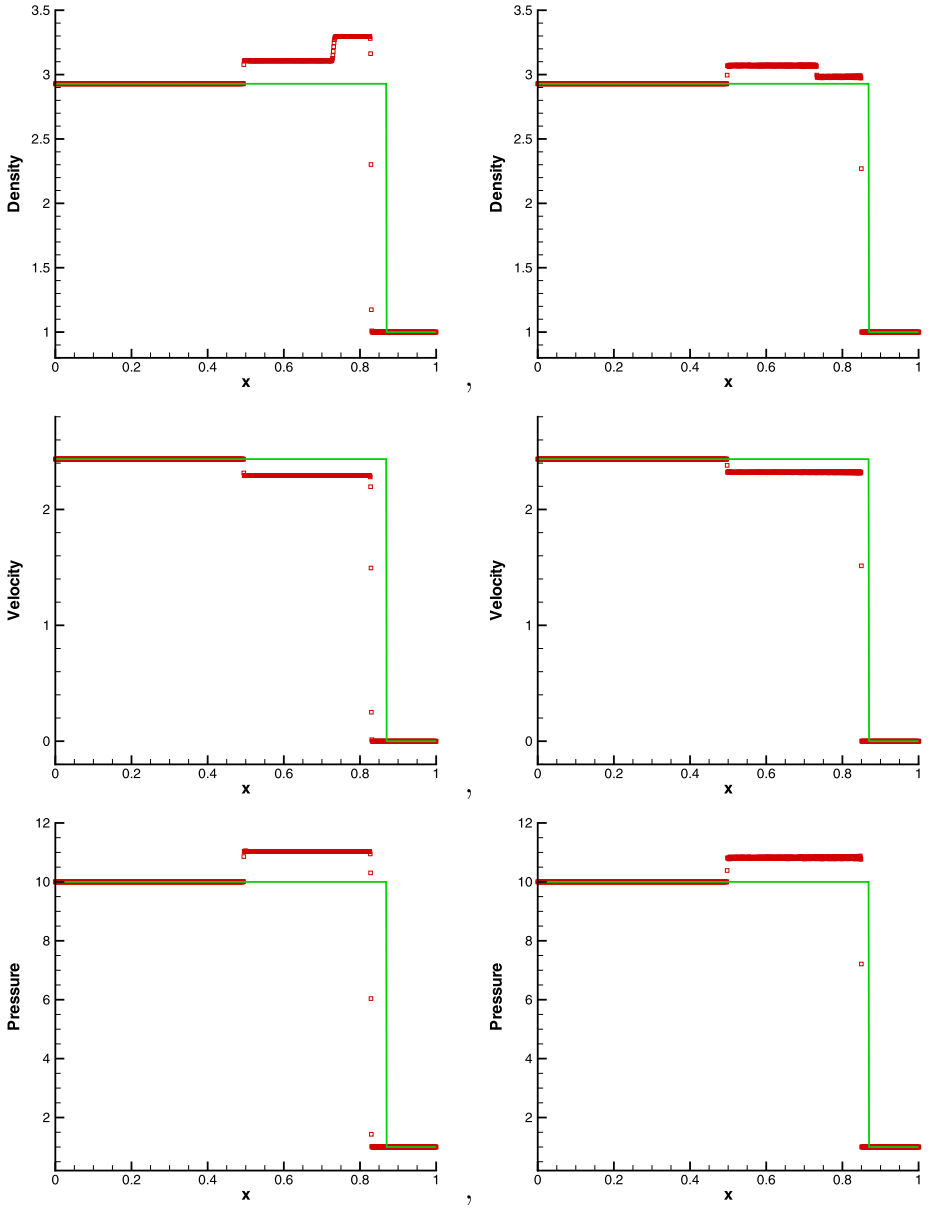

Fig. 3 Density, velocity and pressure for Example 3. $t = 0.1$. $N_x = 1000$. *Solid line*: the exact solution. *Symbol*: the numerical solution. *Left*: exact Riemann solution without subcell resolution; *Right*: subcell resolution and with the line path instead of the exact Riemann solution

$$(\rho, u, p, \gamma) = \begin{cases} (1.3333, 0.3535\sqrt{10^5}, 1.5 \times 10^5, 1.4) & \text{for } x \le 0.05, \\ (1, 0, 1 \times 10^5, 1.4) & \text{for } 0.05 < x \le 0.5, \\ (0.1379, 0, 1 \times 10^5, 5/3) & \text{for } x > 0.5. \end{cases} \tag{8.6}$$

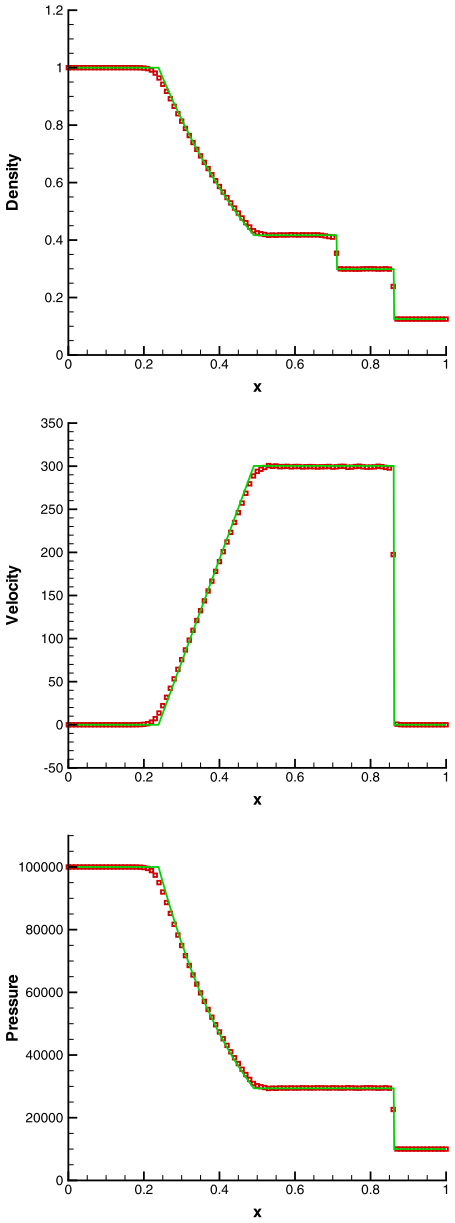

Fig. 4 Density, velocity and pressure for Example 4. $t = 0.0007$. *Solid line*: the exact solution. *Symbol*: the numerical solution

The computed density ρ, velocity u and pressure p are plotted at $t = 0.0012$ against the exact solution in Fig. 6. The strength of the shock for this example is $p_L/p_R = 1.5$, the computed results compare well with the exact solutions, without oscillation around the material interface for the density.

Example 7 This example is the same as Example 6, also taken from [14, 31, 36] only by increasing the strength of the right shock wave to $p_L/p_R = 15$, with the initial condition as:

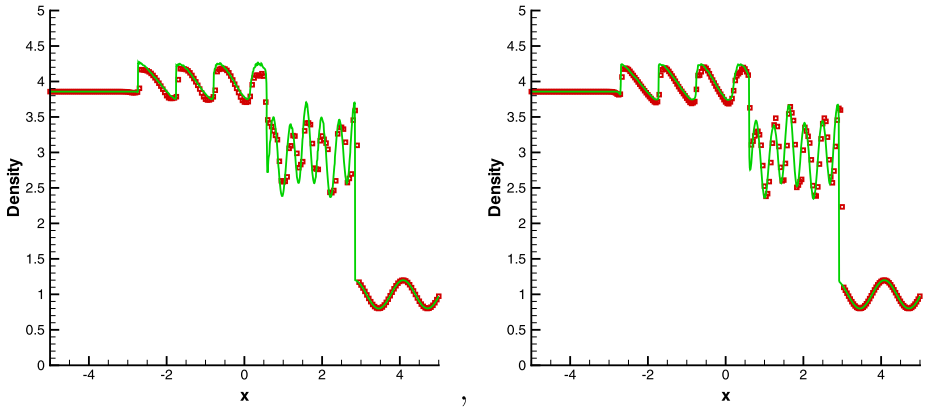

Fig. 5 Density, velocity and pressure for Example 5. $t = 1$. *Solid line*: the converged reference solution for the fifth order method with $N_x = 1000$. *Symbol*: the numerical solution with $N_x = 200$. *Left*: second order method; *Right*: fifth order method

$$(\rho, u, p, \gamma) = \begin{cases} (4.3333, 3.2817\sqrt{10^5}, 1.5 \times 10^6, 1.4) & \text{for } x \le 0.05, \\ (1, 0, 1 \times 10^5, 1.4) & \text{for } 0.05 < x \le 0.5, \\ (0.1379, 0, 1 \times 10^5, 5/3) & \text{for } x > 0.5. \end{cases} \tag{8.7}$$

The computed density ρ, velocity u and pressure p are plotted at $t = 0.0005$ against the exact solution in Fig. 7. The computed results still compare reasonably well to the exact solutions, and there is still no oscillation around the material interface for the density with this stronger strength of the shock. The small glitches on the left constant state can also be observed for the methods in [14, 31, 36], which were explained in [14] to be due to the (mis)capturing of the perfect shock initial data by a shock capturing scheme. In this example, it is more pronounced since the shock wave is much stronger compared to Example 6.

Example 8 This is a problem of a shock wave refracting at an air-helium interface, but with a reflected shock wave [14, 36], with the initial condition as:

$$(\rho, u, p, \gamma) = \begin{cases} (1.3333, 0.3535\sqrt{10^5}, 1.5 \times 10^5, 1.4) & \text{for } x \le 0.05, \\ (1, 0, 1 \times 10^5, 1.4) & \text{for } 0.05 < x \le 0.5, \\ (3.1538, 0, 1 \times 10^5, 1.249) & \text{for } x > 0.5. \end{cases} \tag{8.8}$$

The computed density ρ, velocity u and pressure p are plotted at $t = 0.0017$ against the exact solution in Fig. 8. The computed results show that there are slight oscillations near the left shock region, similar results can also be observed in [14] using the standard scheme from [33]. If we increase the strength of the shock to $p_L/p_R = 15$, the code would blow up. It appears that our subcell resolution procedure is still not accurate enough to capture the strong generated shock during the instant when the original shock wave impacts on the material interface.

Example 9 This is a gas-water shock tube problem with very high pressure in the gaseous medium taken from [31, 36]. The initial condition is given as

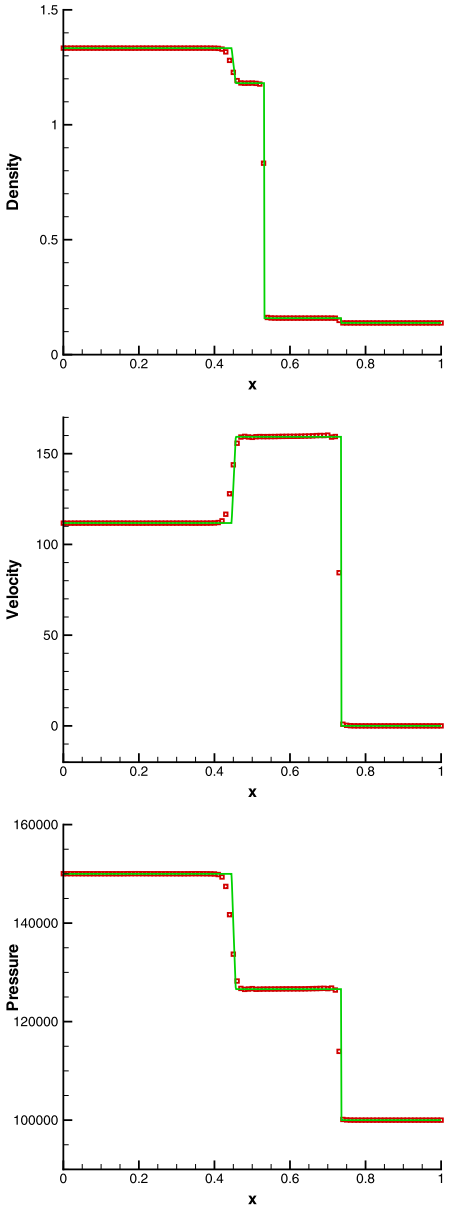

Fig. 6 Density, velocity and pressure for Example 6. $t = 0.0012$. *Solid line*: the exact solution. *Symbol*: the numerical solution

$$(\rho, u, p, \gamma) = \begin{cases} (1270, 0, 8 \times 10^8, 1.4) & \text{for } x \leq 0.5; \\ (1000, 0, 1 \times 10^5, 7.15) & \text{for } x > 0.5. \end{cases} \tag{8.9}$$

The computed density ρ, velocity u and pressure p are plotted at $t = 0.00016$ against the exact solution in Fig. 9. Even though the initial pressure in the gas is extremely high and a very strong shock is generated in the water, our computed results still compare well to the exact solutions.

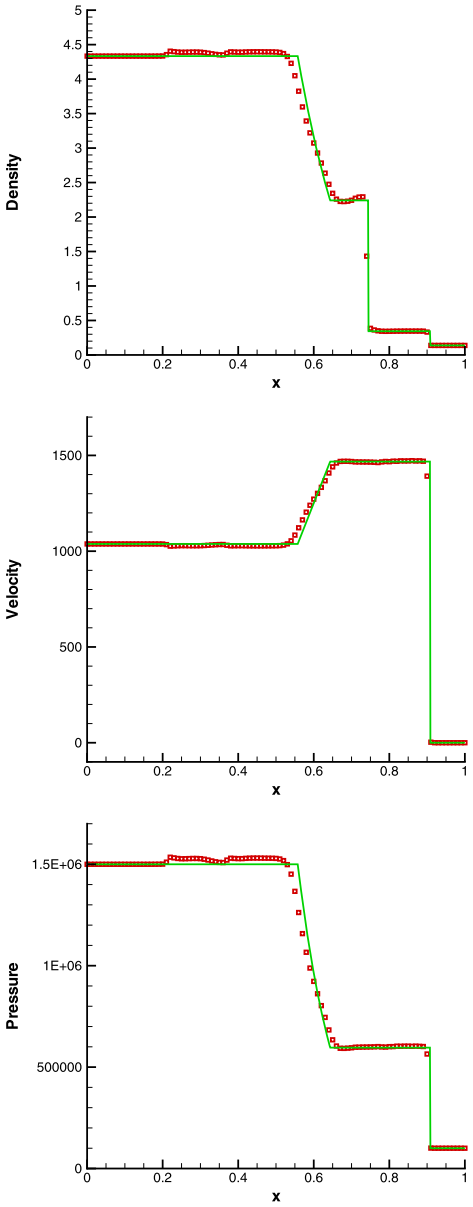

Fig. 7 Density, velocity and pressure for Example 7. $t = 0.0005$. *Solid line*: the exact solution. *Symbol*: the numerical solution

Example 10 This example increases the energy of the explosive gaseous medium in Example 9, which is taken from [14, 31, 36], originally studied in [53] for the underwater explosions, with the initial condition given as

$$(\rho, u, p, \gamma) = \begin{cases} (1630, 0, 7.81 \times 10^9, 1.4) & \text{for } x \leq 0.5; \\ (1000, 0, 1 \times 10^5, 7.15) & \text{for } x > 0.5. \end{cases} \tag{8.10}$$

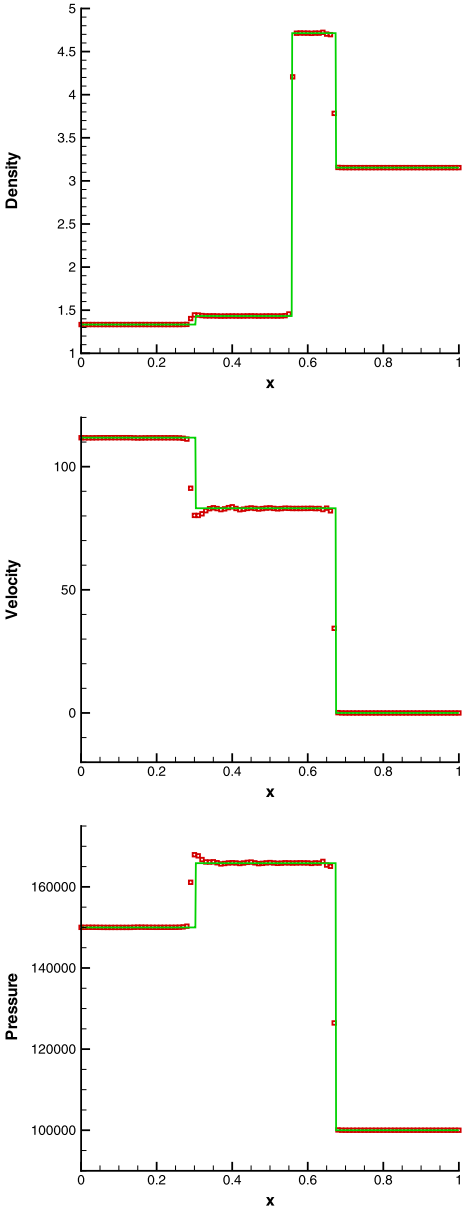

Fig. 8 Density, velocity and pressure for Example 8. $t = 0.0017$. *Solid line*: the exact solution. *Symbol*: the numerical solution

The computed density ρ, velocity u and pressure p are plotted at $t = 0.0001$ against the exact solution in Fig. 10. We begin to see some discrepancies between the exact solution and the numerical solution, however the errors are still reasonably small considering that we are using a nonconservative scheme on this example with very strong discontinuities. The methods in [14, 31, 36] can solve this problem well.

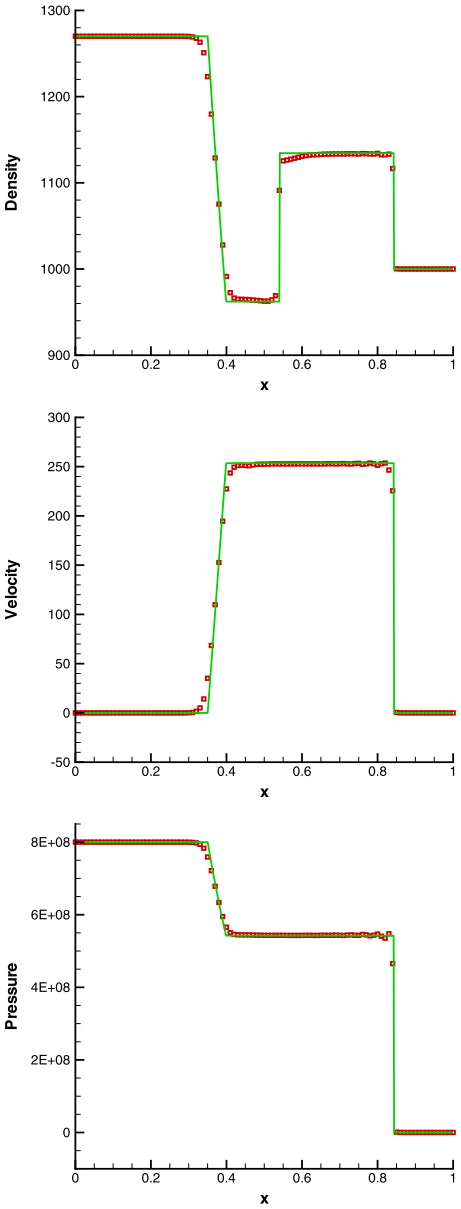

Fig. 9 Density, velocity and pressure for Example 9. $t = 0.00016$. *Solid line*: the exact solution. *Symbol*: the numerical solution

9 Concluding Remarks

In this paper, we have investigated using the WENO reconstruction with a subcell resolution technique when applied to high order Roe-type schemes for nonconservative Euler equations. The subcell resolution is to sharpen discontinuities, in order to remove or significantly reduce transitional points at discontinuities. The technique has been shown to significantly improve the capturing of the correct discontinuity waves by defining the correct path in the path integral at discontinuities. The smearing of discontinuities by shock capturing schemes

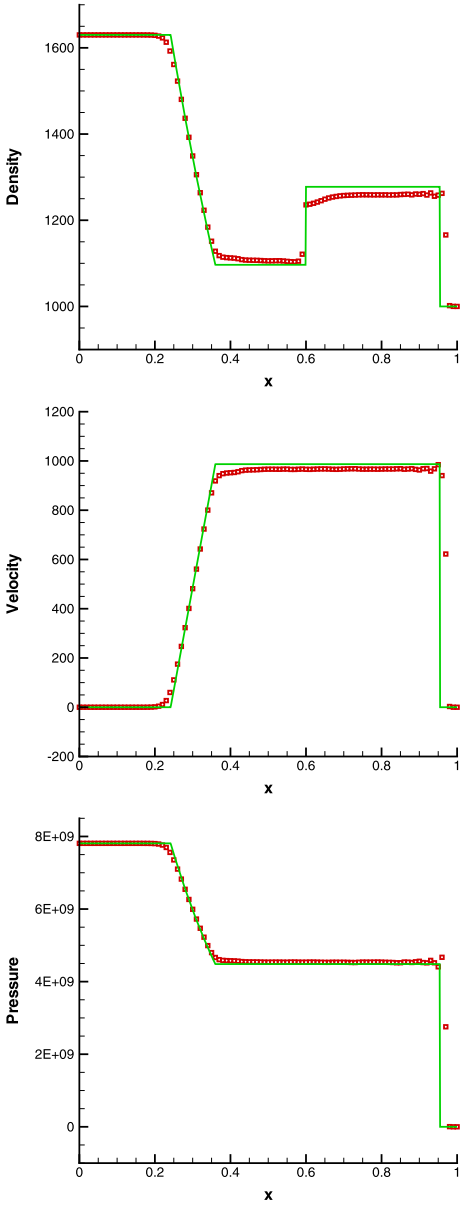

Fig. 10 Density, velocity and pressure for Example 10. $t = 0.0001$. *Solid line*: the exact solution. *Symbol*: the numerical solution

has transitional points at the discontinuities which do not necessarily land on the desired paths. We have identified this numerical smearing as the most probable reason for the failure of schemes to converge to the correct weak solution on the desired paths. The proposed subcell resolution technique within a Runge-Kutta time discretization seems to have robustness problems for very strong discontinuities, especially during interactions of such discontinuities. An improvement on the robustness of the algorithms when transitional points are removed or significantly reduced constitutes our future work.

Our discussion is restricted to the one-dimensional case. A preliminary study on the extension of our methodology to two-dimensional problems (not reported in this paper), implemented in a dimension by dimension fashion (not dimension splitting), has indicated limitations for some of the complex discontinuity wave patterns. This may be due to the complication of two-dimensional waves and the limitation of the subcell resolution technique to capture accurately the correct states and the corresponding paths at the discontinuities. Further investigation of effective multi-dimensional algorithm in this context, for example, discontinuous Galerkin (DG) method [11] and spectral finite volume method [52], also constitutes our future work.

Acknowledgements We would like to thank Dr. Wei Liu for helpful discussions.

References

1. Abgrall, R.: How to prevent pressure oscillations in multicomponent flow calculations: a quasi-conservative approach. J. Comput. Phys. **125**, 150–160 (1996)
2. Abgrall, R., Karni, S.: Computations of compressible multifluids. J. Comput. Phys. **169**, 594–623 (2001)
3. Abgrall, R., Karni, S.: A comment on the computation of non-conservative products. J. Comput. Phys. **229**, 2759–2763 (2010)
4. Adalsteinsson, D., Sethian, J.A.: A fast level set method for propagating interfaces. J. Comput. Phys. **118**, 269–277 (1995)
5. van Brummelen, E.H., Koren, B.: A pressure-invariant conservative Godunov-type method for barotropic two-fluid flows. J. Comput. Phys. **185**, 289–308 (2003)
6. Castro, M.J., Fernández-Nieto, E.D., Ferreiro, A.M., García-Rodríguez, J.A., Parés, C.: High order extensions of Roe schemes for two-dimensional nonconservative hyperbolic systems. J. Sci. Comput. **39**, 67–114 (2009)
7. Castro, M.J., Gallardo, J.M., Parés, C.: High order finite volume schemes based on reconstruction of states for solving hyperbolic systems with nonconservative products. Application to shallow-water systems. Math. Comput. **75**, 1103–1134 (2006)
8. Castro, M.J., LeFloch, P., Muñoz-Ruiz, M.L., Parés, C.: Why many theories of shock waves are necessary: Convergence error in formally path-consistent schemes. J. Comput. Phys. **227**, 8107–8129 (2008)
9. Chen, T.-J., Cooke, C.H.: On the Riemann problem for liquid or gas-liquid media. Int. J. Numer. Methods Fluids **18**, 529–541 (1994)
10. Cocchi, J.-P., Saurel, R.: A Riemann problem based method for the resolution of compressible multimaterial flows. J. Comput. Phys. **137**, 265–298 (1997)
11. Cockburn, B., Shu, C.-W.: The Runge-Kutta discontinuous Galerkin method for conservation laws V: multidimensional systems. J. Comput. Phys. **141**, 199–224 (1998)
12. Dal Maso, G., LeFloch, P., Murat, F.: Definition and weak stability of non-conservative products. J. Math. Pure Appl. **74**, 483–548 (1995)
13. Dumbser, M., Toro, E.F.: A simple extension of the Osher Riemann solver to non-conservative hyperbolic systems. J. Sci. Comput. **48**, 70–88 (2011)
14. Fedkiw, R.P., Aslam, T., Merriman, B., Osher, S.: A non-oscillatory Eulerian approach to interfaces in multimaterial flows (the Ghost Fluid Method). J. Comput. Phys. **152**, 457–492 (1999)
15. Fedkiw, R.P., Marquina, A., Merriman, B.: An isobaric fix for the overheating problem in multimaterial compressible flows. J. Comput. Phys. **148**, 545–578 (1999)
16. Gottlieb, S., Ketcheson, D.I., Shu, C.-W.: High order strong stability preserving time discretizations. J. Sci. Comput. **38**, 251–289 (2009)
17. Harten, A.: ENO schemes with subcell resolution. J. Comput. Phys. **83**, 148–184 (1989)
18. Harten, A., Engquist, B., Osher, S., Chakravarthy, S.: Uniformly high order essentially non-oscillatory schemes, III. J. Comput. Phys. **71**, 231–303 (1987)
19. Harten, A., Hyman, J.M.: Self adjusting grid methods for one-dimensional hyperbolic conservation laws. J. Comput. Phys. **50**, 235–269 (1983)
20. Hou, T.Y., LeFloch, P.: Why nonconservative schemes converge to wrong solutions: error analysis. Math. Comput. **62**, 497–530 (1994)
21. Jiang, G., Peng, D.-P.: Weighted ENO schemes for Hamilton-Jacobi equations. SIAM J. Sci. Comput. **21**, 2126–2143 (2000)

22. Jiang, G., Shu, C.-W.: Efficient implementation of weighted ENO schemes. J. Comput. Phys. **126**, 202–228 (1996)
23. Karni, S.: Viscous shock profiles and primitive formulations. SIAM J. Numer. Anal. **29**, 1592–1609 (1992)
24. Karni, S.: Multicomponent flow calculations by a consistent primitive algorithm. J. Comput. Phys. **112**, 31–43 (1994)
25. Larrouturou, B.: How to preserve the mass fractions positivity when computing compressible multi-component flow. J. Comput. Phys. **95**, 31–43 (1991)
26. LeVeque, R.J.: Finite Volume Methods for Hyperbolic Problems. Cambridge University Press, Cambridge (2004)
27. Liu, T.G., Khoo, B.C., Wang, C.W.: The ghost fluid method for compressible gas-water simulation. J. Comput. Phys. **204**, 193–221 (2005)
28. Liu, T.G., Khoo, B.C., Yeo, K.S.: The simulation of compressible multi-medium flow. Part I: a new methodology with applications to 1D gas-gas and gas-water cases. Comput. Fluids **30**, 291–314 (2001)
29. Liu, T.G., Khoo, B.C., Yeo, K.S.: The simulation of compressible multi-medium flow. Part II: applications to 2D underwater shock refraction. Comput. Fluids **30**, 315–337 (2001)
30. Liu, T.G., Khoo, B.C., Yeo, K.S.: Ghost fluid method for strong shock impacting on material interface. J. Comput. Phys. **190**, 651–681 (2003)
31. Liu, W., Yuan, Y., Shu, C.-W.: A conservative modification to the ghost fluid method for compressible multiphase flows. Commun. Comput. Phys. **10**, 1238–1248 (2011)
32. Liu, X.-D., Osher, S., Chan, T.: Weighted essentially non-oscillatory schemes. J. Comput. Phys. **115**, 200–212 (1994)
33. Mulder, W., Osher, S., Sethian, J.A.: Computing interface motion in compressible gas dynamics. J. Comput. Phys. **100**, 209–228 (1992)
34. Osher, S., Fedkiw, R.P.: Level Set Methods and Dynamic Implicit Surfaces. Springer, Berlin (2003)
35. Parés, C.: Numerical methods for nonconservative hyperbolic systems: a theoretical framework. SIAM J. Numer. Anal. **44**, 300–321 (2006)
36. Qiu, J., Liu, T., Khoo, B.C.: Runge-Kutta discontinuous Galerkin methods for compressible two-medium flow simulations: one-dimensional case. J. Comput. Phys. **222**, 353–373 (2007)
37. Qiu, J., Liu, T., Khoo, B.C.: Simulations of compressible two-medium flow by Runge-Kutta discontinuous Galerkin methods with the Ghost Fluid Method. Commun. Comput. Phys. **3**, 479–504 (2008)
38. Quirk, J.J., Karni, S.: On the dynamics of a shock-bubble interaction. J. Fluid Mech. **318**, 129–163 (1996)
39. Shi, J., Hu, C., Shu, C.-W.: A technique of treating negative weights in WENO schemes. J. Comput. Phys. **175**, 108–127 (2002)
40. Shu, C.-W.: Essentially non-oscillatory and weighted essentially non-oscillatory schemes for hyperbolic conservation laws. In: Cockburn, B., Johnson, C., Shu, C.-W., Tadmor, E. (eds.) Advanced Numerical Approximation of Nonlinear Hyperbolic Equations. Lecture Notes in Mathematics, vol. 1697, pp. 325–432. Springer, Berlin (1998) (Editor: A. Quarteroni)
41. Shu, C.-W., Osher, S.: Efficient implementation of essentially non-oscillatory shock-capturing schemes. J. Comput. Phys. **77**, 439–471 (1988)
42. Shu, C.-W., Osher, S.: Efficient implementation of essentially non-oscillatory shock-capturing schemes II. J. Comput. Phys. **83**, 32–78 (1989)
43. Smoller, J.: Shock Waves and Reaction-Diffusion Equations, 2nd edn. Springer, New York (1994)
44. Sussman, M., Smereka, P., Osher, S.: A level set approach for computing solutions to incompressible two-phase flow. J. Comput. Phys. **114**, 146–159 (1994)
45. Tian, B., Toro, E.F., Castro, C.E.: A path-conservative method for a five-equation model of two-phase flow with an HLLC-type Riemann solver. Comput. Fluids **46**, 122–132 (2011)
46. Tokareva, S.A., Toro, E.F.: HLLC-Type Riemann solver for the Baer-Nunziato equations of compressible two-phase flow. J. Comput. Phys. **229**, 3573–3604 (2010)
47. Toro, E.F.: Riemann Solvers and Numerical Methods for Fluid Dynamics: A Practical Introduction, 3rd edn. Springer, Berlin (2009)
48. Toumi, I.: A weak formulation of Roe's approximate Riemann solver. J. Comput. Phys. **102**, 360–373 (1992)
49. Wang, C.W., Liu, T.G., Khoo, B.C.: A real-ghost fluid for the simulation of multi-medium compressible flow. SIAM J. Sci. Comput. **28**, 278–302 (2006)
50. Wang, C.W., Shu, C.-W.: An interface treating technique for compressible multi-medium flow with Runge-Kutta discontinuous Galerkin method. J. Comput. Phys. **229**, 8823–8843 (2010)
51. Wang, W., Shu, C.-W., Yee, H.C., Sjógreen, B.: High order finite difference methods with subcell resolution for advection equations with stiff source terms. J. Comput. Phys. **231**, 190–214 (2012)

52. Wang, Z.J., Zhang, L., Liu, Y.: Spectral (finite) volume method for conservation laws on unstructured grids IV: extension to two-dimensional Euler equations. J. Comput. Phys. **194**, 716–741 (2004)
53. Wardlaw, A.: Underwater Explosion Test Cases. IHTR 2069 (1998)
54. Xiong, T., Zhang, M., Zhang, Y.-T., Shu, C.-W.: Fast sweeping fifth order WENO scheme for static Hamilton-Jacobi equations with accurate boundary treatment. J. Sci. Comput. **45**, 514–536 (2010)
55. Zhu, J., Qiu, J., Liu, T.G., Khoo, B.C.: RKDG methods with WENO type limiters and conservative interfacial procedure for one-dimensional compressible multi-medium flow simulations. Appl. Numer. Math. **61**, 554–580 (2011)